

# A COMPREHENSIVE STATISTICAL DESCRIPTION OF RADIO-THROUGH- $\gamma$ -RAY SPECTRAL ENERGY DISTRIBUTIONS OF ALL KNOWN BLAZARS

PEIYUAN MAO<sup>1</sup>, C. MEGAN URRY<sup>1</sup>, FRANCESCO MASSARO<sup>1,4,5</sup>, ALESSANDRO PAGGI<sup>2</sup>, JOE CAUTERUCCIO<sup>3</sup> AND SOREN R. KÜNZEL<sup>3</sup>

<sup>1</sup> Yale Center for Astronomy & Astrophysics, Physics Department, New Haven, CT 06520

<sup>2</sup> Harvard-Smithsonian Center for Astrophysics, Cambridge, MA 02138

<sup>3</sup> Department of Statistics, Yale University, New Haven, CT 06520

<sup>4</sup> Physics Department, University of Turin, via Pietro Giuria 1, I-10125 Turin, Italy

<sup>5</sup> Istituto Nazionale di Fisica Nucleare, Sezione di Torino, I-10125 Turin, Italy

*Draft version April 17, 2021*

## ABSTRACT

We combined multi-wavelength data for blazars from the Roma-BZCAT catalog and analyzed hundreds of X-ray spectra. We present the fluxes and Spectral Energy Distributions (SEDs), in 12 frequency bands from radio to  $\gamma$ -rays, for a final sample of 2214 blazars. Using a model-independent statistical approach, we looked for systematic trends in the SEDs; the most significant trends involved the radio luminosities and X-ray spectral indices of the blazars. We used a Principal Component Analysis (PCA), to determine the basis vectors of the blazar SEDs and, in order to maximize the size of the sample, imputed missing fluxes using the K-nearest neighbors method.

Using more than an order of magnitude more data than was available when Fossati et al. (1997, 1998) first reported trends of SED shape with blazar luminosity, we confirmed the anti-correlation between radio luminosity and synchrotron peak frequency, although with greater scatter than was seen in the smaller sample. The same trend can be seen between bolometric luminosity and synchrotron peak frequency. Finally, we used all available blazar data to determine an empirical SED description that depends only on the radio luminosity at 1.4 GHz and the redshift. We verified that this statistically significant relation was not a result of the luminosity-luminosity correlations that are natural in flux-limited samples (i.e., where the correlation is actually caused by the redshift rather than the luminosity).

*Subject headings:* BL Lacertae objects: general, quasars: general, accretion, accretion disks, astronomical databases: miscellaneous

## 1. INTRODUCTION

Blazars are a class of active galactic nuclei (AGN) marked by large amplitude and rapid variability, superluminal motion, and strong non-thermal emission across the entire electromagnetic spectrum from radio to  $\gamma$ -rays (Urry & Padovani 1995). Their spectral energy distributions (SEDs) are dominated by emission from a Doppler-boosted relativistic jet angled close to the line of sight (Blandford & Rees 1978; Urry & Mushotzky 1982). Two distinct blazar subclasses have been defined: flat-spectrum radio quasars (FSRQs), which show strong, broad emission lines in their optical-IR spectra, and BL Lac objects, which have weak or no emission lines (equivalent widths  $EW < 5\text{\AA}$ ; Angel & Stockman 1980; Stocke et al. 1985; Landt et al. 2001).

Blazar SEDs are characterized by two broad components, the low frequency one produced by synchrotron radiation from relativistic electrons in the jet, and the high frequency one produced by inverse Compton scattering of ambient photons by those same electrons (Urry & Padovani 1995; Abdo et al. 2010). Blazars with synchrotron peaks at high frequency (HSPs, with  $\nu_{peak} > 10^{15}\text{Hz}$ , see Abdo et al. 2010) have been found primarily in X-ray surveys, while low-synchrotron-peaked blazars (LSPs, with  $\nu_{peak} < 10^{14}\text{Hz}$ ) have been found preferentially in radio and GeV  $\gamma$ -ray surveys (Giommi & Padovani 1994; Stocke et al. 1985; Maraschi et al. 1986; Fichtel et al. 1994). In the early blazar samples, the syn-

chrotron peak frequencies were anti-correlated with luminosity (Stocke et al. 1985; Sambruna et al. 1996; Fossati et al. 1997; Giommi & Padovani 1994). However, these studies were based on more than  $\sim 130$  objects, with at most 34 (Fossati et al. 1998) having  $\gamma$ -ray data, so the full range of luminosity and redshift was not well sampled.

With the launch of *Fermi* satellite (Ackermann et al. 2011), GeV  $\gamma$ -ray data are now available for more than 1000 blazars, along with extensive multi-wavelength data at radio, infrared, optical and X-ray wavelengths. In this paper, we characterize the SEDs of 2214 blazars for which redshifts and substantial wavelength coverage are available, using a non-parametric statistical approach. While this sample is not complete in a formal sense, it is a far larger sample with far more comprehensive SED data than most previous studies (Fossati et al. 1997, 1998 cf. Giommi et al. 2013.) In Section 2, we describe the sample and the data collected at various wavelengths. Since much of the X-ray data were previously unpublished, we also include a description of the X-ray data reduction. In Section 3 we use statistical analysis to find the most significant correlations displayed in the data, free from any assumed functional form. Throughout the paper, the energy spectral index,  $\alpha$ , is the power-law exponent of the flux density defined by  $F_\nu \propto \nu^{-\alpha}$ , which makes the photon index  $\Gamma = \alpha + 1$ . The cosmological parameters  $H_0 = 70 \text{ km s}^{-1}\text{Mpc}^{-1}$  and  $\Omega_\Lambda = 0.72$  (Hinshaw et al. 2013) are used. All references of the logarithmic function are in base 10.

## 2. SAMPLE SELECTION

We base our blazar sample on the data in the Multi-wavelength Catalog of blazars, Roma-BZCAT<sup>1</sup> v5.0, released in December 2014, which is the most comprehensive catalog in the literature, (Massaro et al. 2009, 2011a, 2014a) with 3561 blazars and blazar candidates. The Roma-BZCAT catalog includes: 1151 BL Lac objects (named BZBs in Roma-BZCAT), of which 1059 are spectroscopically confirmed (i.e., the spectra show no emission lines with  $EW > 5\text{\AA}$ ), and another 92 are candidates (i.e., they have been classified as BL Lacs in the literature but spectroscopic data are not in the published literature; 1909 radio-loud quasars with flat radio spectra (BZQs); 227 blazars of uncertain type (BZUs, adopted for sources with peculiar characteristics<sup>2</sup>); and 274 potential BL Lac objects which have optical spectra dominated by galaxy emission instead of non-thermal emission (BZGs, see Massaro et al. 2012). Further details about the Roma-BZCAT selection and classification criteria, together with the list of the surveys on which it is based, can be found in (Massaro et al. 2009, 2011a, 2014a).

Since the main goal of our study is to investigate the shapes of blazar SEDs, and to identify their possible dependences on luminosity and redshift, we considered only BZBs and BZQs for which a firm redshift<sup>3</sup> is known. This reduces our sample to 2220 sources, including 1880 BZQs and 340 BZBs (not surprisingly, only a third of the 1059 BZBs have redshifts); the 92 BL Lac candidates are not included because we want a clean sample not contaminated by sources of uncertain type. Cross-matching with other multi-wavelength surveys, all 2220 were detected in the radio band (that being one of their defining characteristics), most were detected in the near-IR, slightly fewer than half have counterparts in the optical, about one third have X-ray data, and just under a quarter were detected in  $\gamma$ -rays. Below we describe the data used in each wavelength band.

### 2.1. Radio Data

For 1992 blazars, radio flux densities at 1.4 GHz are available from the NRAO VLA Sky Survey (NVSS) (Condon et al. 1998) and/or the Faint Images of the Radio Sky at Twenty Centimeters (FIRST) survey (Becker et al. 1995; White et al. 1997). The NVSS surveyed the 82% of the celestial sphere at declinations  $\delta \geq -40^\circ$  with a flux limit of  $\sim 2.5$  mJy and an angular resolution of  $\sim 45''$ , while FIRST covers 10,000  $\text{deg}^2$  in the northern hemisphere to a sensitivity limit of  $\sim 1$  mJy with an angular resolution of  $\sim 5''$ .

For another 224 sources, Roma-BZCAT provides the flux density at 843 MHz from the Sydney University Moolonglo Sky Survey (SUMSS) (Mauch et al. 2003), which covers 3500  $\text{deg}^2$  of the southern sky with  $\delta \leq -30^\circ$  with mosaic resolution of  $45'' \times 45'' \text{ cosec}|\delta|$  and a limiting

flux of 2-3 mJy, similar to the NVSS. In order to compare the sources on equal footing, we need a frequency sampling as uniform as possible and interpolate these values to 1.4 GHz assuming the power-law spectral index measured between 843 MHz and 5 GHz (the slope of a linear fit between 0.843 and 5 GHz in  $\log \nu - \log \nu L_\nu$  plane). Two of these 224 sources did not have 5 GHz fluxes reported, and another 4 sources have only 5 GHz fluxes reported; these 6 were not included in our sample since interpolation to 1.4 GHz was not possible.

For all but 158 of the 2214 blazars, the radio flux density at 5 GHz is also available in the Roma-BZCAT (the actual band center is at 4.85 GHz). The 158 missing blazars are preferentially low redshift objects with faint radio fluxes at 1.4 GHz (blue points in Figure 1), meaning that either their 5 GHz fluxes are below the NVSS or FIRST sensitivity thresholds, or they have higher positional uncertainties so the cross-matches between two frequencies are more difficult. Clearly these are among the lowest luminosity blazars in the sample.

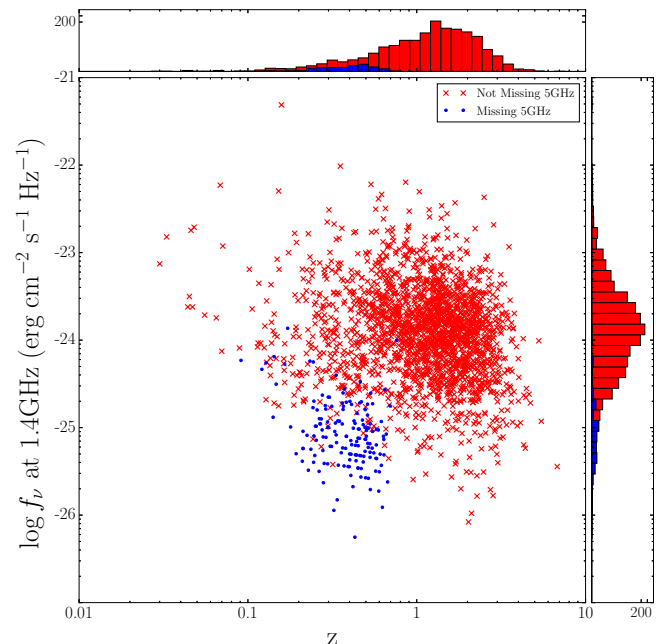


FIG. 1.— Radio flux at 1.4 GHz vs. redshift for blazars with (red crosses) or without (blue circles) 5 GHz data, and the associated one-dimensional histograms. The blazars missing 5 GHz fluxes are generally at lower redshift and lower luminosity than the rest of the sample.

### 2.2. Infrared Data

The WISE (Wide-field Infrared Survey Explorer) all-sky survey, released in November 2013 as the ALLWISE catalog<sup>4</sup>, covers the entire sky at 3.4, 4.6, 12, and 22  $\mu\text{m}$ , with angular resolutions of 6.1'', 6.4'', 6.5'' and 12.0'', respectively. The  $5\sigma$  photometric sensitivity is estimated to be 0.068, 0.098, 0.86 and 5.4 mJy (16.6, 15.6, 11.3, 8.0 Vega mag), respectively, in unconfused regions on the ecliptic plane. We converted the reported WISE magni-

<sup>1</sup> <http://www.asdc.asi.it/bzcat/>

<sup>2</sup> For instance, occasional presence/absence of broad spectral lines or features, transition objects between a radio galaxy and a BL Lac, or galaxies hosting a low luminosity blazar nucleus. Refer to <http://www.asdc.asi.it/bzcat/> for details

<sup>3</sup> Redshift without the '?', '??', '>' flags, where flags indicate uncertainty in the value ('?'), extreme uncertainty ('??') or a lower limit ('>'). Refer to <http://www.asdc.asi.it/bzcat/> for details.

<sup>4</sup> <http://wise2.ipac.caltech.edu/docs/release/allwise/>

tudes<sup>5</sup> to flux densities using zero-magnitude flux densities of 309.540 Jy (W1), 171.787 Jy (W2), 31.674 Jy (W3) and 8.363 Jy (W4), respectively. We also corrected the reported WISE magnitudes for Galactic absorption using the Draine (2003) relation and values of  $N_H$  from Kalberla et al. (2005); and applied the color corrections from Wright et al. (2010, Table 1).

Cross-matching our blazar sample with the WISE survey, adopting an optimal radius of  $3.3''$  (D’Abrusco et al. 2013; Massaro et al. 2013; D’Abrusco et al. 2014), we find that 2151 out of 2214 sources in our sample have a mid-IR counterpart. All 2151 are detected in at least the first two WISE bands at  $3.4 \mu\text{m}$  and  $4.6 \mu\text{m}$ ; 2019 were also detected at  $12 \mu\text{m}$ ; and 1628 have a counterpart in all four filters. No blazars had more than one WISE counterpart within  $3.3''$  and the probability of spurious association of any one WISE source with a BZCAT source is lower than 3% (D’Abrusco et al. 2013).

We note that 1478 sources of the 2151 with a WISE counterpart also have a counterpart in the 2MASS catalog, but these data were not included in our analysis because the 2MASS data have a much brighter flux limit than WISE, in part because the sky background is so much higher from the ground.

### 2.3. Optical Data

The Sloan Digital Sky Survey (SDSS) covers more than 8000 square degrees of the sky in five optical band-passes, centered at 354.3 nm, 477 nm, 623.1 nm, 762.5 nm and 914.3 nm (called *u*, *g*, *r*, *i*, *z*; Stoughton et al. 2002). We used SDSS AB magnitudes from Data Release 9 (Ahn et al. 2012), and converted to flux densities<sup>6</sup> using a zero-point flux density of 3631 Jy. The SDSS covers only about one quarter of the sky but more than half the Roma-BZCAT sample (1238 objects) lies in its footprint because of an observational bias toward the northern hemisphere.

Adopting an association radius of  $1.8''$ , which provides a probability of spurious associations lower than 1% for a match between any Roma-BZCAT source and an SDSS DR9 source (Massaro et al. 2014b), we find that 963 of 1238 blazars have an SDSS counterpart. For our work we included only the 432 SDSS sources that have the following flags<sup>7</sup> equal to 1: CLASS\_OBJECT (i.e., primary object) and CODE\_MISC (i.e., clean photometry for point source).

Although SDSS officially reports fluxes in 5 bands, we did not include the u-band flux in our analyses, since it is the least sensitive band and is very likely affected by “big blue bump” (thermal emission from an optically thick accretion disk feeding the central black hole, see Shields 1978) in many blazars, especially FSRQs. We also excluded magnitudes below the completeness limits (22.2 for *g* and *r* bands, 21.3 for *i* band and 20.5 for *z* band<sup>8</sup>), as these data tend to be unreliable and could greatly affect the other optical bands due to their contribution to calculating the *K* corrections in the remaining bands. Removing them reduces the number of blazars

with SDSS counterparts to 407. As in the case of WISE cross-matching, no double counterparts were found.

### 2.4. X-Ray Data

The Swift X-Ray Telescope (XRT) is a focusing X-ray telescope with a  $110 \text{ cm}^2$  effective area,  $18''$  resolution and an energy range  $0.2 - 10 \text{ keV}$ , with a flux limit of  $2 \times 10^{-14} \text{ erg cm}^{-2} \text{ s}^{-1}$  for a  $10^4$ -second observation (Burrows et al. 2005).

Searching for X-ray counterparts of the 2214 blazars in the Swift archive<sup>9</sup>, we found 700 sources with an X-ray detection above  $3\sigma$ . The Swift sky coverage is far from uniform, with some blazars being observed repeatedly and others not having been observed yet; observations of previously unobserved blazars have been proposed.

The 34 X-ray-brightest sources generate pile-ups in the Swift detectors (this occurs whenever two or more photons are detected as a single event, and we take the threshold to be when the count rate exceeds 0.4 counts per second). Detailed Swift analyses for these objects were reported in two earlier papers (Massaro et al. 2008, 2011b), from which we took the normalization at 1 keV and the spectral index.

Another 157 X-ray sources have count rates  $< 0.4$  counts per second but a substantial number of total counts, i.e.,  $> 400$ . We analyzed these Swift data with the XRT Interactive Tool provided at the ASDC-BZCAT website, using the response matrix for the Swift XRT Burrows et al. (2005). The tool runs XSPEC with a power-law model with absorbing column density,  $N_H$ , frozen at the Galactic value (taken from <http://heasarc.gsfc.nasa.gov/cgi-bin/Tools/w3nh/w3nh.pl>; Kalberla et al. 2005) after binning the data into 6 energy bins, and yields a best-fit normalization (flux density at 1 keV) and spectral index. As a check, we compare the fitted spectral index to that estimated from the measured hardness ratio (discussed below).

Fig. 2 shows that the spectral index derived from the hardness ratio is systematically steeper than the fitted index, by about  $\Delta\alpha \sim 0.2$ , comparable to the root mean square (rms) deviation and well within the systematic uncertainties. A rescaling has been applied to all HR-derived spectral indices to correct for this difference.

For the remaining 509 blazars that were too faint for spectral analysis (total counts  $< 400$ ), we derived the spectral index from the hardness ratio, defined as  $\text{HR} \equiv (\text{H-S})/(\text{H+S})$ , where H and S are the counts in the hard ( $2 - 10 \text{ keV}$ ) and soft ( $0.5 - 2 \text{ keV}$ ) bands, respectively (Evans et al. 2014). Specifically, we re-ran the Swift XRT pipelines and generated the calibrated event files and exposure maps for each blazar, and measured the number of counts in the soft ( $0.5-2 \text{ keV}$ ) and hard ( $2-10 \text{ keV}$ ) bands, from which we calculated the hardness ratio. We then used PIMMS (Mukai 1993), taking into account of the Swift XRT response, to calculate the flux density at 1 keV using the obtained spectral index and the total count rate.

### 2.5. $\gamma$ -Ray Data

<sup>5</sup> <http://wise2.ipac.caltech.edu/docs/release/allwise/expsup/index.html>

<sup>6</sup> <http://www.sdss3.org/dr9/algorithms/fluxcal.php>

<sup>7</sup> See description of flags at <http://cas.sdss.org/dr7/sp/help/browser/browser.asp?n=PhotoObj>.

<sup>8</sup> <https://www.sdss3.org/dr9/scope.php>

<sup>9</sup> <http://swift.gsfc.nasa.gov/archive/>

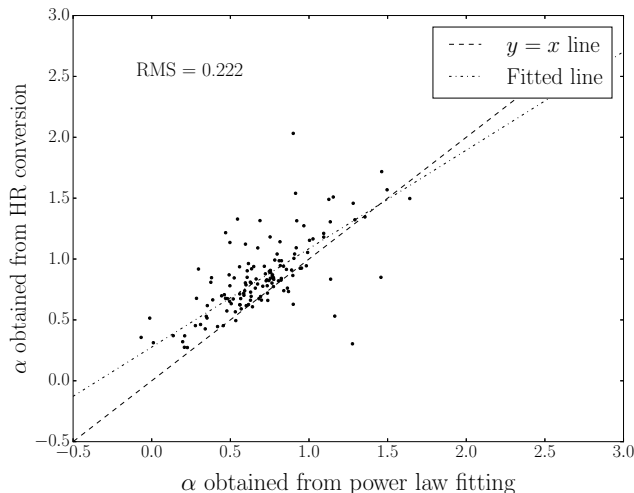


FIG. 2.— Comparison of spectral indices obtained for moderately bright sources from the hardness ratio (HR) and from directly fitting a power law with XSPEC. The HR-derived index is systematically steeper than the fitted index, but the offset is comparable to the rms dispersion ( $\Delta\alpha = 0.222$ ) and well within the larger uncertainty introduced by the degeneracy of  $\alpha$  and  $N_H$ . A correction is applied to all HR-derived spectral indices to correct for this difference.

We obtained  $\gamma$ -ray data for 571 of the 2214 blazars from the *Fermi* Third LAT Sources Catalog<sup>10</sup> (3FGL, Acero et al. 2015). The LAT (Large Area Telescope) is a silicon strip detector sensitive to  $\gamma$ -rays in the energy range from 20 MeV to more than 300 GeV (Atwood et al. 2009); the associations with the Roma-BZCAT were already provided in the 3FGL (3LAC, the counterpart coordinates were used to find the best cross-matches with the latest version of the BZCAT).

The *Fermi* catalog lists integrated fluxes, in units of photons per unit area per unit time, in 5 energy bands: 100 MeV–300 MeV, 300 MeV–1 GeV, 1 GeV–3 GeV, 3 GeV–10 GeV and 10 GeV–100 GeV. The best-fit photon index across the entire  $\gamma$ -ray spectrum,  $\Gamma$ , is also reported there in Acero et al. (2015). We did not require detections in all 5 bands; instead, we derived the monochromatic flux density at 1 GeV (which is near the peak of the *Fermi* LAT sensitivity) from  $\Gamma$  and the reported flux (integrated from the 100 MeV to 100 GeV range).

### 2.6. Multi-Wavelength Data

We collected available fluxes for the following 12 frequencies:

- 2 in radio: 1.4 GHz, 5 GHz;
- 4 from infra-red (WISE): W1, W2, W3, W4;
- 4 from optical (SDSS): g, r, i, z;
- 1 in X-ray: 1 keV; and
- 1 in  $\gamma$ -ray: 1 GeV.

All flux densities were converted to the same units,  $\text{erg cm}^{-2} \text{s}^{-1} \text{Hz}^{-1}$ . We then applied a K correction using the formula  $F_{\nu, \text{corr}} = F_{\nu} \cdot (1+z)^{\alpha-1}$  where  $\alpha$  is

the spectral index at frequency  $\nu$ . For SDSS and WISE,  $\alpha$  comes from fitting a local power law between adjacent bands and taking into account the color-color corrections; for  $\gamma$ -rays,  $\alpha$  comes from the  $\Gamma$  values reported by Acero et al. (2015).

Note that for 102 blazars the  $\gamma$ -ray spectrum was fitted as a log parabola instead of the usual power law, where  $\frac{dN}{dE} = K \left(\frac{E}{E_0}\right)^{-\alpha-\beta \log E/E_0}$  (Acero et al. 2015). We computed their fluxes accordingly and applied a modified K correction consistent with the spectral shape ( $F_{\nu, \text{corr}} = F_{\nu} \cdot (1+z)^{1-\alpha-\beta \log(1+z)}$ ). K-corrected fluxes were converted to luminosities, and to characterize the SED shapes, we fit to  $\log \nu L_{\nu}$  (see Section 3).

We estimated the frequencies of the synchrotron component by fitting a second order polynomial to the radio-through-optical SED, for the 1590 blazars with radio data and complete optical or complete infrared data.

In summary, our sample includes: 2214 blazars (1876 BZQs, 338 BZBs; this sums to less than the radio sample because we excluded 6 objects which had fluxes only at 5 GHz), of which 2151 have WISE data, 407 have SDSS counterparts, 700 have Swift XRT data, and 571 have *Fermi* LAT data. Only 54 blazars have complete data across all frequencies. Table 1 and Figure 3 summarize the multi-wavelength data available for the sample; the complete data of our blazar collection is in a machine readable format online, a sample of which is shown in Table 2.

TABLE 1  
DATA COMPLETENESS SUMMARY

Band	Sources <sup>a</sup>	$L_{\text{min}}$ <sup>b</sup>	$L_{\text{max}}$ <sup>c</sup>
z	2214	0.03	6.802
1.4GHz	2214	39.71	45.49
5GHz	2056	40.57	45.89
W4	1628	42.89	48.32
W3	2019	42.93	48.08
W2	2151	43.14	48.20
W1	2151	43.09	49.16
z	407	43.66	47.47
i	407	43.65	47.30
r	407	43.64	48.69
g	407	43.64	49.12
X-Ray	700	42.28	47.21
$\gamma$ -Ray	571	42.89	48.70

<sup>a</sup>Number of objects with data available

<sup>b</sup>Minimum value of  $\log(\nu L_{\nu})$  for the subsample detected in each band, in ergs/s.

<sup>c</sup>Maximum value of  $\log(\nu L_{\nu})$  for the subsample detected in each band, in ergs/s.

## 3. STATISTICAL INVESTIGATION

In this section we characterize blazar spectral energy distributions using a variety of statistical analyses to determine the most significant trends. The idea is to base this characterization on the data rather than fitting arbitrary functional forms to the SEDs.

### 3.1. Clustering Analysis

Previous works showed that radio luminosities of blazars are anti-correlated with the frequencies of their

<sup>10</sup> [http://fermi.gsfc.nasa.gov/ssc/data/access/lat/4yr\\_catalog/](http://fermi.gsfc.nasa.gov/ssc/data/access/lat/4yr_catalog/)

TABLE 2  
THE COMPLETE DATA FOR ALL BLAZARS <sup>a</sup>

<sup>a</sup>The full sample table contains 20 columns and 2214 rows, and is available in a machine readable format online.

BZCAT name	WISE name	Fermi name	R.A. (degs)	Dec (degs)	Redshift	1.4 GHz (erg s <sup>-1</sup> )
BZBJ0945+5757	J094542.20+575747.6	3FGL J0945.9+5756	146.425958333	57.96325	0.229	41.2999741162
BZBJ0002-0024	J000257.17-002447.2	N/A	0.738166666667	-0.413083333333	0.523	42.3071693579
BZBJ0006-0623	J000613.88-062335.2	N/A	1.557875	-6.39311111111	0.347	42.9106779635
BZBJ0008-2339	J000835.40-233927.8	3FGL J0008.6-2340	2.14741666667	-23.6577222222	0.147	40.3985164399
BZBJ0013+1910	J001356.37+191041.9	N/A	3.48483333333	19.1783333333	0.477	42.0567302367
BZBJ0017+1451	J001736.90+145101.7	N/A	4.40375	14.8505277778	0.303	41.2671294407
BZBJ0021-0900	J002142.25-090044.4	N/A	5.42604166667	-9.01230555556	0.648	41.8362628391
BZBJ0032-2849	J003233.08-284920.4	3FGL J0032.3-2852	8.13779166667	-28.8223055556	0.324	41.7686091928
BZBJ0040-2719	J004016.42-271911.7	N/A	10.068375	-27.3198888889	0.172	41.1872720594
BZBJ0047+3948	J004755.22+394857.5	3FGL J0048.0+3950	11.9800833333	39.816	0.252	41.3333179422

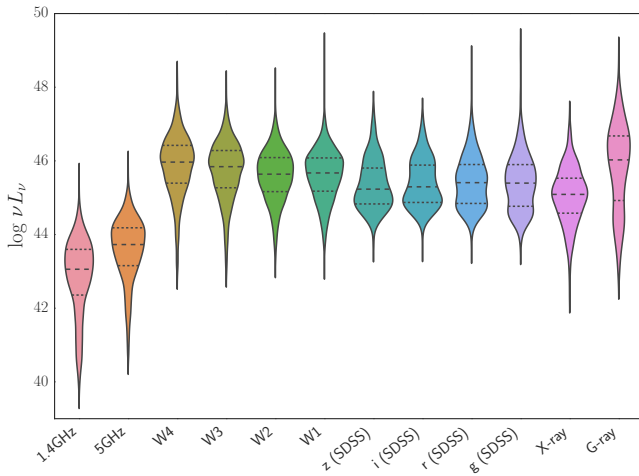


FIG. 3.— Violin plot of the blazar sample, showing their luminosity distributions ( $\log \nu L_\nu$ ). The three dotted lines in each “violin” shows the 25th, 50th and 75th percentiles. Note that each “violin” is normalized to the same area, i.e., the shaded area does not represent the relative number of objects in each band.

synchrotron peaks (Sambruna et al. 1996; Fossati et al. 1997, 1998). In our much larger sample, we see the same trend between radio luminosity and the synchrotron peak in the SED. Specifically, Figure 4 illustrates the anti-correlation between radio luminosity and the synchrotron peak; the large scatter in the latter is partly due to the difficulty in defining the peak frequency from fewer than a dozen data points. The bolometric luminosity is similarly anti-correlated with synchrotron peak (Figure 5), with no sharp distinction between BL Lacs and FSRQs.

Figure 6 shows the SEDs of the 2214 blazars with radio, infrared and optical data, sorted into five bins of radio luminosity (roughly 200 to 700 objects per bin). The anti-correlation of synchrotron peak with luminosity is visible, even though a big blue bump from an accretion disk (at high luminosities) and host galaxy emission (in the lowest luminosity bin) are comparable to the synchrotron contribution. The analytic form Fossati et al. (1998) fitted to 126 blazar SEDs, only 34 of which included  $\gamma$ -ray fluxes, does not fit the more extensive data. Neither are the data well fit by the updated parameters of Donato et al. (2001), although the fit to the  $\gamma$ -ray data

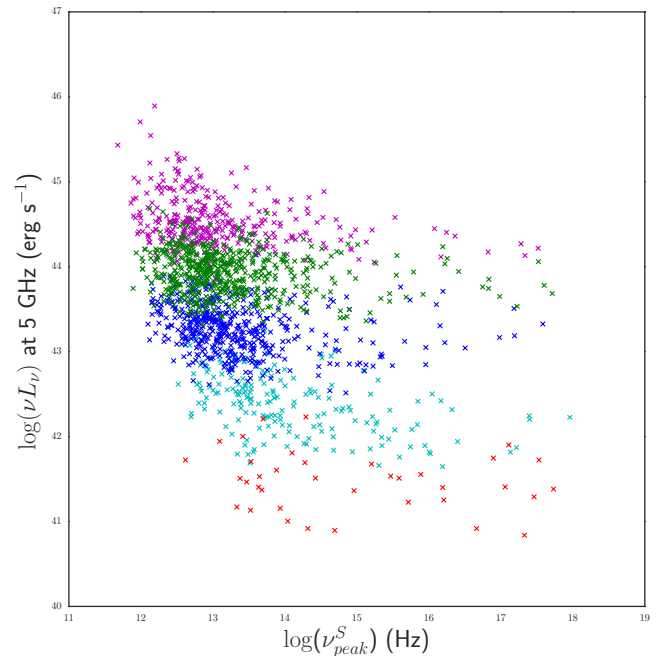


FIG. 4.— Radio luminosity versus synchrotron peak frequency for the 1590 blazars with radio data and complete optical or complete infrared data, with colors defined by the radio luminosity bins in Figure 6. The synchrotron peaks were determined via a second order polynomial fit to the radio-through-optical SED, and are probably uncertain by at least one decade (obtained by refitting and measuring the shift in peaks after removing WISE or SDSS data from the 54 complete SEDs with well-defined peaks). Even with large scatter, the synchrotron peak frequency rises smoothly as the radio luminosity decreases (coefficient of correlation  $\rho = -0.476$ ).

is slightly better. 2160 of 2214 blazars lack data in one or more bands; we show in Section 3.2.2 that the blazars with missing data are not significantly different from the blazars that have those data, and so their absence does not affect the overall SED shape.

The SEDs for this large sample are not as well separated as the well-known plots from Fossati et al. (1998, Figure 12) may have made them appear; outside the radio band (which by definition has distinct bins), the SEDs overlap substantially, as indeed they did in the original Fossati sample. In other words, the scatter at

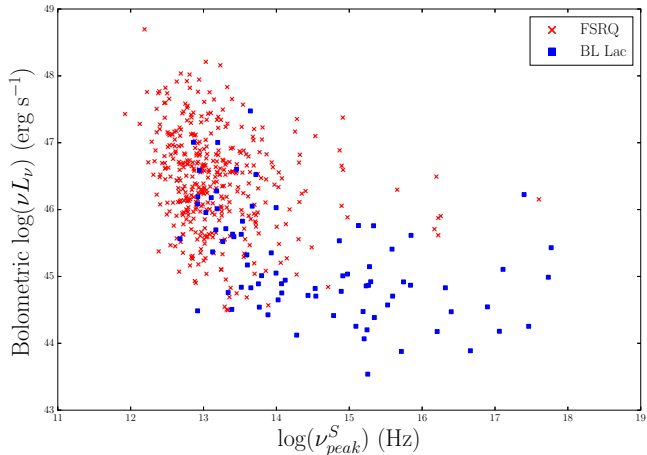


FIG. 5.— Bolometric luminosity versus synchrotron peak frequency for the 480 blazars with full radio, infrared and optical data. 401 red crosses represent flat-spectrum radio quasars (i.e., blazars with broad emission lines) and the 79 blue filled squares are BL Lacs (i.e., with no or weak emission lines). Bolometric luminosity was determined from the peak  $\nu L_\nu$  value; note that this is essentially the  $\gamma$ -ray luminosity for low-frequency-peaked, luminous blazars, or the X-ray luminosity for high-frequency-peaked BL Lac objects. As in Figure 4, synchrotron peak frequencies were found via a second order polynomial fit to the radio-through-optical SED. The same anti-correlation of synchrotron peak with luminosity is seen ( $\rho = -0.533$ ), and there is no particular separation of FSRQs and BL Lacs, although the former are more luminous on average than the latter.

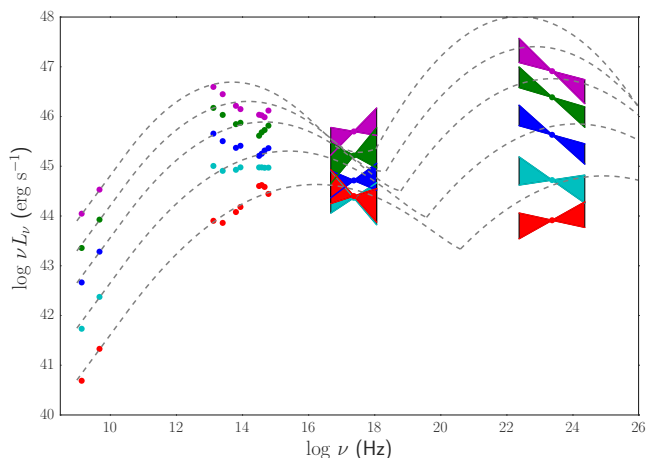


FIG. 6.— Spectral energy distributions of 2214 blazars sorted into five bins of radio luminosity (purple, red, green, cyan, and blue, in order of decreasing luminosity at 1.4 GHz); these were the natural clusters of K-nearest neighbors, with 200 to 700 objects per luminosity bin of a decade or less in luminosity. Median luminosity and X- and  $\gamma$ -ray slopes are plotted for each bin, with one standard deviation uncertainties. The anti-correlation of synchrotron peak with luminosity is visible, although a big blue bump (at high luminosities) and host galaxy emission (in the lowest luminosity bin) are comparable to the synchrotron contribution. The analytic form SED proposed by Fossati et al. (1998) based on 126 blazars (*dashed lines*) clearly does not fit the more extensive data.

optical or  $\gamma$ -ray wavelengths is larger than the scatter within a given radio luminosity bin. Furthermore, the clustered SEDs differ significantly from the analytic Fossati et al. (1998) curve.

The blazar sample can also be sorted naturally — and slightly differently — by X-ray spectral index, as illus-

trated in Figure 7. The X-ray spectral index varies through a large range, depending on whether the low-energy or high-energy SED component is dominant. If the synchrotron radiation dominates at X-ray energies, the X-ray spectrum falls steeply with increasing frequency (decreasing wavelength); if instead a Compton-scattered component dominates, the X-ray flux rises with frequency. The different X-ray slopes are reminiscent of the Fossati et al. (1998) SED pattern (even though that was based on a radio sorting), with high-luminosity, low-frequency-peaked blazars having hard X-ray spectra that are part of the Compton-scattered component, and low-luminosity, high-frequency-peaked blazars having soft X-ray spectra that are the high-energy tail of the synchrotron component.

The trend of SED shape with blazar luminosity is clearly seen, with the more  $\gamma$ -ray luminous objects having low-frequency synchrotron peaks and hard X-ray spectra, and the less luminous objects having high-frequency synchrotron peaks and soft X-ray spectra. A plot of the individual (unbinned) SEDs is shown in Figure 8. These shapes are not easily described by an analytic formula, even generalizing from Fossati et al. (1997), nor is the scatter as small as that work suggested. Accordingly, we looked for a general way to describe the SED shapes and their trends with luminosity.

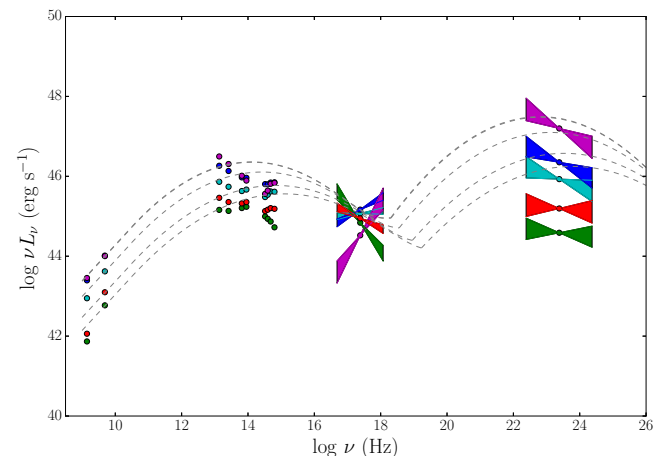


FIG. 7.— Blazar SEDs binned according to X-ray spectral index, showing the clear trend of hardening X-ray spectral index with increasing radio luminosity. The median luminosity in each bin and the median X- and  $\gamma$ -ray slopes are plotted, with one standard deviation uncertainties. The analytic SED shape proposed by Fossati et al. (1998), keyed to the 5 GHz radio frequency bin (*dashed lines*), does not fit the data.

### 3.2. Multi-band correlations

#### 3.2.1. Principal Component Analysis

Principal Component Analysis (PCA) is a useful non-parametric method that can be applied to find correlations among fluxes at different wavelengths. Briefly, PCA finds and orders the strongest correlations in an  $n$ -dimensional space (here  $n = 12$ ), and returns the basis vectors and their associated variances. By definition, the components, or basis vectors, are orthogonal to one another and thus uncorrelated. The appropriate number of



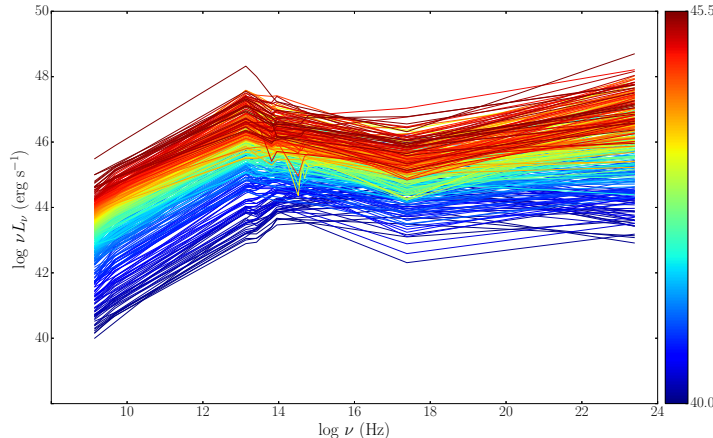


FIG. 8.— Individual SEDs of 347 blazars that have radio, X-ray and  $\gamma$ -ray data, and either WISE or SDSS data (or both). Data points are connected using straight lines without binning in order to avoid any assumption about the SED shape. The color is scaled to the radio luminosity. The overall trend of decreasing synchrotron peak with increasing luminosity is clear, as is the large dispersion around the average SED shape.

basis vectors is always less than or equal to the dimensionality of the original space. In short, PCA redefines the axis of the parameter space so that the basis vectors best define the trends inherent in the data.

We first performed PCA on the set of 54 blazars with complete data across all 12 bands, in order to obtain a reference set of basis vectors to help guide subsequent analyses. Table 3 lists the coefficients for each of the four dominant basis vectors, as well as the associated standard deviations, fractional variance and cumulative variance.

TABLE 3  
COEFFICIENTS AND VARIANCES OF BASIS VECTORS FOR 54 COMPLETE BLAZAR SEDS

Band	BV 1	BV 2	BV 3	BV 4
1.4GHz	-0.36978	0.23622	0.4954	-0.28891
5GHz	-0.36674	0.20313	0.3554	-0.14724
W4	-0.33667	0.23729	-0.2406	0.33268
W3	-0.32203	0.18565	-0.2515	0.30176
W2	-0.27201	0.06799	-0.2697	0.22561
W1	-0.27406	0.02293	-0.259	0.12514
z	-0.22425	-0.46464	0.2136	0.25268
i	-0.22964	-0.40565	0.1093	0.10032
r	-0.23103	-0.32775	0.0894	0.06374
g	-0.22527	-0.29663	0.1485	0.05732
X-Ray	-0.19481	-0.35295	-0.3604	-0.51569
$\gamma$ -Ray	-0.33585	0.1946	-0.2496	-0.48532
Std Dev	2.498	0.69322	0.45604	0.38181
Prop. Var. <sup>a</sup>	0.844	0.06501	0.02814	0.01972
Cum Var. <sup>b</sup>	0.844	0.90901	0.93714	0.95687

<sup>a</sup>The variance each basis vector contributes to the total variance.

<sup>b</sup>The cumulative variance of all previous basis vectors.

The first basis vector, which depends approximately equally on all 12 fluxes, carries 84% of the total variance in the data. The second basis vector depends differently on the optical and X-ray fluxes (change of sign) and explains another 6% of the variance; the third basis vector

emphasizes the radio, X-ray and  $\gamma$ -ray data. Together, the first four basis vectors explain 96% of the total variance in the blazar SEDs.

We were concerned that the optical fluxes might include a contribution from host galaxy light (in low-luminosity blazars) or from a luminous UV-emitting accretion disk (in high-luminosity blazars) that are thermal component contaminations not related to the blazar SED shape we are investigating. Accordingly, we repeated the PCA analysis excluding the SDSS data, and indeed, the first basis vector now explains a slightly higher fractional variance (89%); in other words, the SEDs are slightly more uniform without the (possibly unrelated) optical points. The sense of the second basis vector is also different, with opposite dependence on radio luminosity and with much higher variance, suggesting that the radio band indeed carries more information about the nonthermal jet emission than the other bands. The coefficients and significances of these basis vectors (i.e., without SDSS data) are listed in Table 4.

TABLE 4  
COEFFICIENTS AND VARIANCES OF EACH BASIS VECTOR FOR 338 BLAZARS WITH COMPLETE DATA APART FROM SDSS

Band	BV 1	BV 2	BV 3	BV 4
1.4GHz	-0.38915	0.39474	0.41777	0.06506
5GHz	-0.3929	0.35039	0.31293	0.08492
W4	-0.38571	0.01232	-0.27929	0.13689
W3	-0.3668	-0.02357	-0.27423	0.18416
W2	-0.30624	-0.09628	-0.21904	0.26454
W1	-0.2984	-0.12845	-0.17257	0.24365
X-Ray	-0.21285	-0.65685	0.65246	-0.00855
$\gamma$ -Ray	-0.42001	-0.27236	-0.24951	-0.70395
Std Dev	2.5732	0.52681	0.45663	0.36484
Prop. Var. <sup>a</sup>	0.8901	0.03731	0.02803	0.01789
Cum Var. <sup>b</sup>	0.8901	0.92738	0.95541	0.9733

<sup>a</sup>The variance each basis vector contributes to the total variance.

<sup>b</sup>The cumulative variance of all previous basis vectors.

It is also possible that the thermal dust torus emission or even the accretion disk contributes to the infrared data. We subsequently performed a PCA analysis without the WISE data, and found that the proportional variance of first basis vector drops to 80% from the original 84%, indicating a loss of information on correlation and not the removal of an independent component like a torus. The coefficients and significances of these basis vectors are listed in Table 5. Plotkin et al. (2012) discussed in detail that the BL Lacs do not have thermal torus emission in WISE.

### 3.2.2. Assessing the effect of missing data on estimates of SED shape

We want to use existing data to study blazar SEDs and to form an estimator for SED shape using the observed correlations. However, with data that are basically flux-limited, the absence of data in a given band might not be uncorrelated with that object's SED shape.

In particular, many of the blazars in our sample lack data in one or more of the 12 bands, with only 54 having data in every band. Instead of restricting the sample to that handful of objects, it makes sense to use all the

TABLE 5  
COEFFICIENTS AND VARIANCES OF EACH BASIS VECTOR FOR  
BLAZARS WITH COMPLETE DATA APART FROM WISE

Band	BV 1	BV 2	BV 3	BV 4
1.4GHz	-0.46281	0.3921	-0.22	0.24046
5GHz	-0.45512	0.3287	-0.1758	0.20664
z	-0.29242	-0.404	-0.2508	-0.56169
i	-0.29397	-0.3677	-0.1297	-0.1048
r	-0.2922	-0.2975	-0.1239	0.15678
g	-0.28642	-0.2529	-0.1662	0.12781
X-Ray	-0.24781	-0.336	0.499	0.48837
$\gamma$ -Ray	-0.41324	0.2712	0.6718	-0.47021
Std Dev	1.9729	0.65106	0.4172	0.36496
Prop. Var. <sup>a</sup>	0.8073	0.08792	0.0361	0.02763
Cum Var. <sup>b</sup>	0.8073	0.89522	0.9313	0.95894

<sup>a</sup>The variance each basis vector contributes to the total variance.

<sup>b</sup>The cumulative variance of all previous basis vectors.

available information but only after ascertaining that the partial data do not bias the sample.

We first plot several histograms comparing objects with and without data in a specific band. In Fig. 9 we show the particular case of blazars with and without X-ray data. As is evident from the dotted, dashed and dot-dash lines in the plot (corresponding to the 25th, 50th and 75th percentiles), the two subgroups have visually different distributions. A series of Kolmogorov-Smirnov (KS) tests were carried out, and test statistics are given in Table 6.

While every band (other than radio at 1.4 GHz) has some missing data, missing optical data are in fact the worst problem, as only 432 blazars have complete SDSS photometry<sup>11</sup> (the fewest of all wavelengths). By comparing the coefficients and the variances of the PCA basis vectors in Tables 3 and 4, it is clear that the intrinsic correlations among the SED bands did not change much after the SDSS data were removed. In other words, the 338 blazars with complete data excepting the optical have SEDs that are essentially indistinguishable from the 54 full-data blazars.

We then repeated the PCA analysis to assess the effect of missing  $\gamma$ -ray data, since only 571 blazars (measured redshifts) have Fermi data. For the 98 blazars with complete data excepting the  $\gamma$ -ray, the basis vectors again had similar coefficients and variances, thus indicating they are indistinguishable from the 54 full-data blazars.

Table 7 shows the coefficients for the first basis vector for blazars that have complete data minus one or more bands. The significance of each basis vector and the overall PCA result does not change much if one or more bands are excluded. This indicates that the overall SED shapes with and without certain bands do not look very different, i.e., the blazars with missing data do not strongly bias the results.

### 3.3. Imputation

Since PCA works only with complete data (by the nature of the algorithm), we considered measures to fill in the missing data. Two methods, namely, Multiple Imputation and Sequential K-Nearest Neighbors, were tried.

<sup>11</sup> The number is roughly as expected given the SDSS footprint compared to the area of radio- and  $\gamma$ -ray-surveyed sky.

Multiple Imputation is a model-based approach to estimating the potential value of a missing data point. A series of iterative regression analyses were run in which one particular band was used as the dependent variable and the other bands were used as independent variables. The regression model was generated with all available data, and if the dependent band had any missing values, these values were estimated by the regression using data from all the other bands.

We saw unphysical results from the Multiple Imputation approach, where many of the correlation plots showed strange vertical and/or horizontal strips (see Figure 10, panels *a*, *c*, *e*).

These linear features look very different from the original data, due to the fact that Multiple Imputation uses data from all 12 bands of all 2214 blazars to over-specify the structure to the point that the model does not have enough freedom to produce useful predictions; instead, it produces repetitive predicted fluxes in line with the populated information.

Sequential K-Nearest Neighbors (KNN), on the other hand, imputes a missing data point from the closest  $k$  data in an  $(N - 1)$ -dimensional space defined by the vectors not being considered. In our analysis, we used the generally assumed number value of  $k = 10$  (Feigelson & Jogesh Babu 2012). Other  $k$  values did not produce better results. The imputed value of the missing point is equal to the inverse distance-weighted mean of its its neighbor’s values, and the distance measures considered here are “statistical” distances, i.e., the mean and the co-variance.

Sequential KNN gave much better results than Multiple Imputation, as the imputed data very nicely follow the form of the originally populated values as we would have expected (Figures 10 and 11, panels *b*, *d*, *f*).

One potential drawback of KNN is that it mimics our data in *every* respect, reducing the variance artificially. We proceed using the KNN method to impute missing data, and interpret the results with appropriate caution. Figure 11 shows the 2-band correlations with real and imputed data.

We next ran the PCA analysis on the real plus imputed data. As expected, the variance explained by the first basis vector is larger because KNN-imputed data mimic the original data. Coefficients and significances of the newly generated basis vectors are shown in Table 8.

This PCA result shows the same correlations as for the original 54-complete blazars. Of course, it does rely heavily on those 54 blazars, but in fact this PCA uses available data from almost every single blazar, and the result is far more representative and less biased. And the fact that the first basis vector still explains approximately 88% of the variation in our original data tells us that all the bands load more or less evenly on this basis vector.

The remaining basis vectors give us a sense of the natural band grouping and indicate how much explanatory power these groups provide on their own. Since the second basis vector is dominated by the radio bands, considering the radio in its own right is an important step.

Figure 12 shows the same array of SEDs as in Figure 8 but including the KNN-imputed data. The anti-correlation between radio luminosity and synchrotron



TABLE 6  
KOLMOGOROV-SMIRNOV PROBABILITY OF VALUES DRAWN FROM THE SAME DISTRIBUTION

Band <sup>a</sup>	Redshift	1.4 GHz	5 GHz	W4	W3	W2	W1	z	i	r	g	X-ray	$\gamma$ -ray
WISE	1.3e-17	1.4e-18	0.0e+00	NA	NA	NA	NA	1.3e-01	1.5e-01	1.2e-01	4.0e-07	5.3e-17	2.7e-07
SDSS	1.5e-02	1.5e-01	6.5e-01	4.8e-01	3.5e-01	1.2e-01	5.9e-293	NA	NA	NA	NA	3.6e-01	4.2e-01
X-ray	4.2e-06	2.7e-05	3.0e-11	1.7e-06	1.8e-06	1.6e-06	1.8e-06	1.2e-01	1.8e-01	6.6e-02	6.2e-02	NA	5.8e-73
$\gamma$ -ray	1.9e-02	8.5e-03	5.6e-18	1.1e-17	1.8e-17	2.2e-17	1.5e-01	4.3e-01	3.5e-01	5.6e-01	2.7e-83	0.0e+00	NA

<sup>a</sup>The rows are bands omitted, and the columns are bands in consideration

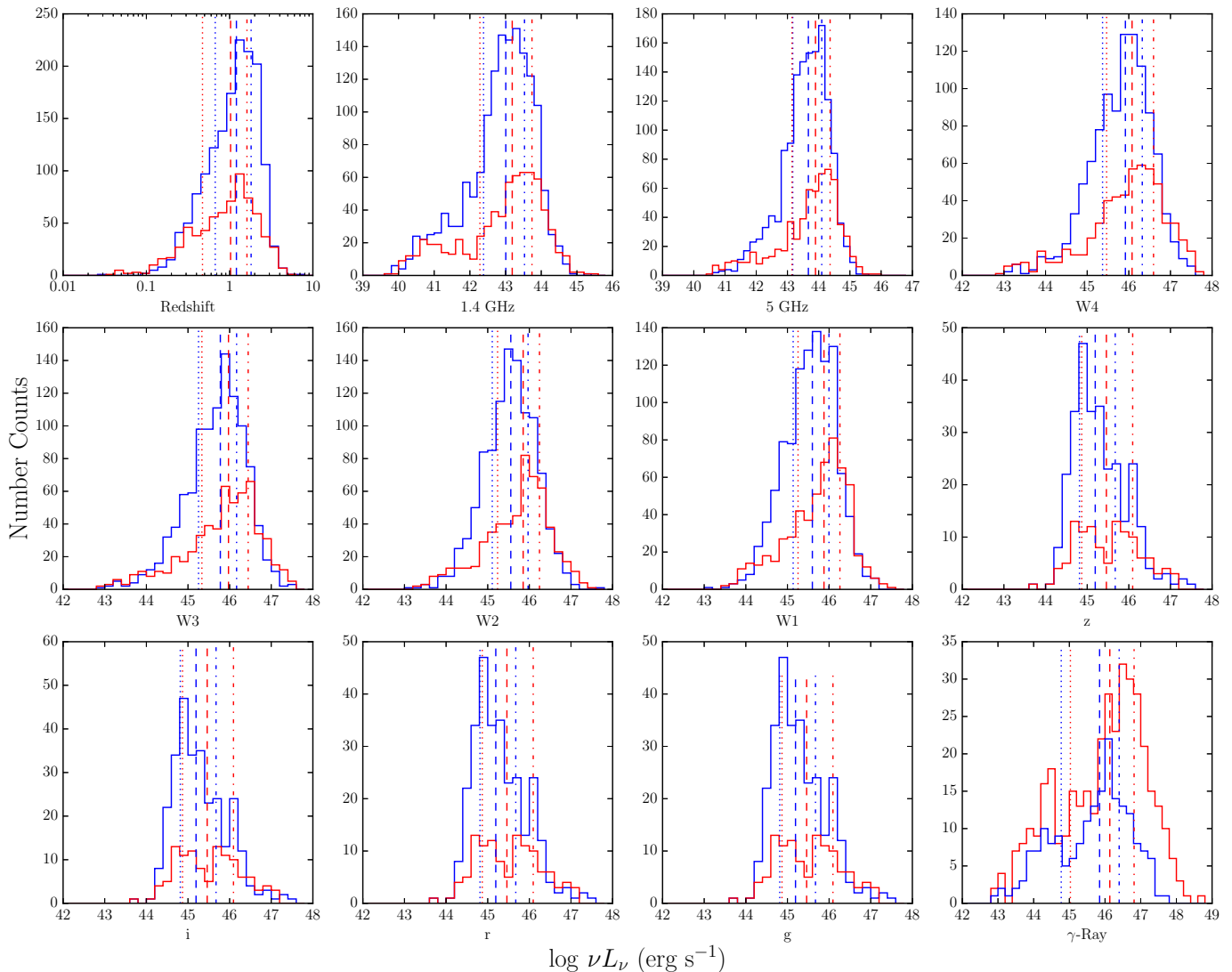


FIG. 9.— Histograms comparing the multiwavelength flux distributions of blazars with (*red*) and without (*blue*) X-ray data. The vertical lines indicate the mean fluxes (*dashed lines*) and the 25th (*dotted lines*) and 75th percentiles (*dot-dash lines*).

peak is preserved, as expected.

#### 4. ESTIMATORS

Given the analysis presented in above, we now describe an estimator for blazar luminosity at any wavelength based on the radio luminosity at 1.4 GHz. Although we could use a different band as the input for an estimator (because the PCA analysis shows different wavebands to be highly correlated), using 1.4 GHz maximizes our completeness.

The resultant functional form, obtained using the standard theory of linear models, is a first order polynomial in radio luminosity ( $\log(\nu L_\nu)$  at 1.4 GHz) and redshift ( $\log(1+z)$ ):

$$\log(\nu L_\nu) = c_0 + c_1 \log(1+z) + c_2 \log(\nu L_{\nu 1.4\text{GHz}}).$$

The complete coefficients are listed in Table 9.

Figure 13 shows the residuals after applying the estimator to all blazars for which data are available in a particular band. The predicted estimator values were sub-

TABLE 7  
VALUES OF BASIS VECTOR 1 FOR SAMPLES MISSING DATA IN VARIOUS BANDS

Omitted bands	None	SDSS	$\gamma$ -ray	X-ray	SDSS & $\gamma$ -ray	SDSS & X-ray	$\gamma$ -ray & X-ray	SDSS, $\gamma$ -ray & X-ray
# blazars	54	338	98	83	561	492	293	1603
1.4 GHz	-0.36978	-0.38915	-0.39152	-0.36792	0.43105	-0.39492	-0.43995	-0.3944
5 GHz	-0.36674	-0.39290	-0.38858	-0.36582	0.43476	-0.39925	-0.44396	-0.3912
W4	-0.33667	-0.38571	-0.35585	-0.33694	0.42352	-0.39699	-0.43835	-0.3597
W3	-0.32203	-0.36680	-0.34062	-0.32370	0.40302	-0.37845	-0.41804	-0.3456
W2	-0.27201	-0.30624	-0.28843	-0.27459	0.33706	-0.31661	-0.35014	-0.2938
W1	-0.27406	-0.29840	-0.29007	-0.27791	0.32809	-0.30996	-0.34242	-0.2968
z	-0.22425	NA	-0.24102	-0.23598	NA	NA	NA	-0.2537
i	-0.22964	NA	-0.24565	-0.24235	NA	NA	NA	-0.2596
r	-0.23103	NA	-0.24708	-0.24458	NA	NA	NA	-0.2623
g	-0.22527	NA	-0.24128	-0.24051	NA	NA	NA	-0.2584
X-ray	-0.19481	-0.21285	-0.20706	NA	0.23285	NA	NA	NA
$\gamma$ -ray	-0.33585	-0.42001	NA	-0.35645	NA	-0.43074	NA	NA
Prop. Var. <sup>a</sup>	0.844	0.8901	0.8452	0.8419	0.890	0.9255	0.9342	0.8435

<sup>a</sup>The fractional variance of the first basis vector.

TABLE 8  
COEFFICIENTS AND VARIANCES OF EACH BASIS VECTOR FOR ORIGINAL PLUS KNN-IMPUTED DATA

Band	BV 1	BV 2	BV 3	BV 4
1.4GHz	-0.4075	0.549	0.3379	0.0221
5GHz	-0.40487	0.4616	0.1664	0.00598
W4	-0.37366	-0.1263	-0.3949	0.37292
W3	-0.36218	-0.1712	-0.2914	0.10959
W2	-0.30287	-0.2446	-0.0519	-0.30574
W1	-0.27747	-0.2725	0.0128	-0.55548
X-Ray	-0.22374	-0.4419	0.6861	0.06391
$\gamma$ -Ray	-0.41438	-0.1836	-0.1529	0.14074
Std Dev	2.3654	0.58008	0.38865	0.287
Prop. Var.	0.8834	0.05313	0.02385	0.013
Cum Var.	0.8834	0.93654	0.96039	0.9734

TABLE 9  
COEFFICIENTS FOR THE ESTIMATOR

Band	$c_0$	$c_1$	$c_2$	$\sigma$ <sup>a</sup>
5GHz	5.692	0.614	0.876	0.173
W4	27.977	3.085	0.393	0.39
W3	28.593	3.03	0.376	0.355
W2	30.955	2.464	0.322	0.366
W1	30.358	1.874	0.341	0.422
i	39.29	2.822	0.121	0.455
r	38.909	2.838	0.131	0.402
g	38.967	3.199	0.127	0.434
z	37.824	3.311	0.153	0.476
X-Ray	37.762	2.458	0.152	0.518
$\gamma$ -Ray	22.961	3.934	0.508	0.42

<sup>a</sup>Standard deviations in the Gaussian fit to the residuals of the estimator.

tracted from the measured values to produce the residuals. The results are distributed in a well-behaved Gaussian around a mean value of zero, showing that the estimator is correctly predicting the distributions of blazar luminosities.

A discussion of the origin of the correlations, which serves as the theoretical underpinning of this estimator,

is in Section 5. Better estimation with smaller residuals is of course possible by increasing the degrees of freedom by adding more input terms, but our goal is not to fit perfectly each SED but to have a robust estimator that captures the general SED trends for the full population of blazars. With this estimator, the luminosity of any blazar with known radio luminosity and redshift can be predicted across  $\sim 15$  decades of the electromagnetic spectrum. Such an estimator could be used, for example, to model the blazar population as a whole.

Finally, to test the efficiency/reliability of the statistical estimator (previously defined) we performed the following test. We considered the radio luminosities of the sources listed in our original blazar sample, and computed the expected values of the fluxes (K-corrected) at different frequencies and compared them with the observed values within a  $3\sigma$  interval. The reliability derived from this cross-validation test are reported in Table 10 for each energy range, respectively.

The reliability represents the fraction of sources for which the estimator correctly predicts the flux within  $3\sigma$  in a particular band. We note that blazars tend to be highly variable objects, especially in the higher energy frequency bands, and in addition, our large sample undoubtedly includes intrinsic scatter that was not as visible in the smaller samples studied previously. The discrepancy between the predicted and actual luminosities reflects both variational and real difference. However, our goal is to correct distribution for the overall blazar population, not to recover accurate SEDs for individual objects, and the estimator, which is built on the largest and most complete collection of blazars to date, successfully achieves this goal.

## 5. DISCUSSIONS AND CONCLUSIONS

In this paper, we have characterized SEDs of 2214 blazars with complete redshift information, using data from Roma-BZCAT, the largest and the most complete collection of known blazars. Compared with previous work on blazar demographics (Giommi & Padovani 1994; Stocke et al. 1985; Maraschi et al. 1986; Fichtel et al. 1994; Nieppola et al. 2006; Chen & Bai 2011; Meyer et al. 2011; Ghisellini et al. 2011; Giommi et al. 2012, 2013),

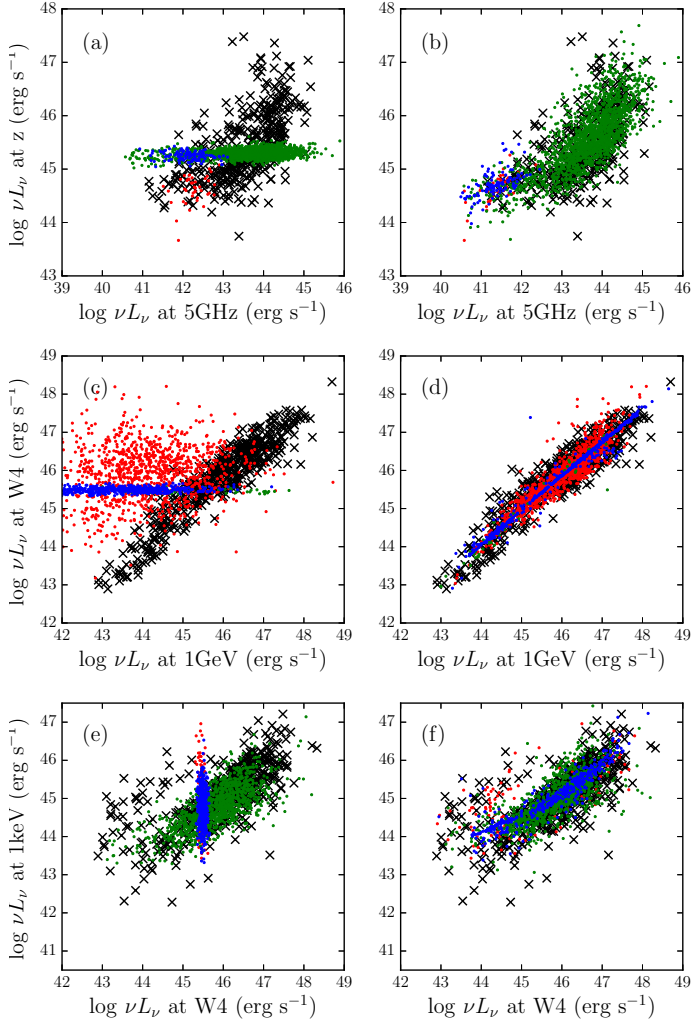


FIG. 10.— Some of the correlation plots of Multiple Imputation (*left*) and K-nearest Neighbors (*right*) using all the data available (up to 12 bands). In these plots, the black crosses are data complete in both bands, red dots are imputed data originally missing in the band on the  $x$ -axis; green dots are imputed data originally missing in the  $y$ -axis. Blue dots are imputed data missing in both plotted bands. The Multiple Imputation approach creates trends not present in the original data (horizontal and vertical strips), while the KNN-imputed values follow the existing trends.

this represents the largest sample with more, and more uniform, data from radio through  $\gamma$ -ray energies.

Of the 2214 blazars in our sample, all have measured radio luminosities at 1.4 GHz, 2056 have measured radio luminosities at 5 GHz, 1628 have infrared fluxes across all four WISE bands (W1, W2, W3, W4), 432 have optical luminosities from SDSS (g, r, i, z), 700 have X-ray luminosities at 1 keV, and 571 have  $\gamma$ -ray luminosities at 1 GeV.

Through non-parametric analysis of these blazar SEDs, we have confirmed the connection between radio luminosity and SED shape, such that the synchrotron peak frequency decreases as the radio (also bolometric) luminosity increases. Principal component analysis showed that the first basis vector depends on the luminosities at various wavelengths, with roughly equal contributions to the variance; this shows that 90% of the correlation is explained by the bolometric luminosity. In the second basis

TABLE 10  
RELIABILITY OF THE ESTIMATOR IN RESPECTIVE ENERGY BANDS

Band	Reliability <sup>a</sup>
W4	68.8%
W3	58.5%
W2	16.9%
W1	7.92%
z	32.2%
i	15.3%
r	3.64%
g	2.60%
X-ray <sup>b</sup>	9.80%
$\gamma$ -ray	14.0%

<sup>a</sup>The reliability represents the fraction of sources for which the estimator correctly predicts the flux within  $3\sigma$  in a particular band

<sup>b</sup>An interval of  $1\sigma$  is used for X-ray since the errors in count rates are relatively big compared with the count rates themselves and using  $3\sigma$  would result in unphysical answers for many objects.

vector, the radio luminosities are the dominant contributors to the variance (and have opposite sign to the other luminosities), meaning it is reasonable to use the radio luminosity as the driving parameter.

We constructed a non-parametric estimator of the blazar SED based on the radio luminosity (at 1.4 GHz) and the redshift, which are a key part of the first basis vector signal. In a subsequent paper, this estimator will be combined with the 1.4-GHz radio luminosity function to study blazar demographics (Mao et al., in preparation).

The SED trends we observe, called the “blazar sequence” by Fossati et al. (1998) and Ghisellini et al. (1998), has been discussed extensively (see Ghisellini & Tavecchio 2008; Ghisellini et al. 2009, 2011, 2012, Giommi et al. 1999, 2012, 2013, Nieppola et al. 2006, 2008 and Chen & Bai 2011). Meyer et al. (2011) extended the idea of the blazar sequence to a broader “blazar envelope”, which bounds two populations: highly aligned blazars with high synchrotron peaks (at all luminosities) and misaligned radio galaxies with low synchrotron peaks and low luminosities.

The observed trends in blazar SED shape were explained theoretically by Ghisellini et al. (1998) using a simple synchrotron inverse-Compton model. Specifically, in luminous blazars with high photon energy densities due to accretion disk and line emission, the synchrotron-radiating electrons lose energy through Compton up-scattering, producing strong  $\gamma$ -ray components and lower synchrotron peak frequencies, while the electron energy distribution remains hard in less luminous BL Lac objects, which lack strong line emission, producing high-frequency synchrotron peaks and low  $\gamma$ -ray luminosities. Thus the blazar sequence can be explained naturally.

However, if high-luminosity, high-synchrotron-peak blazars are systematically missing from major surveys, then the observed trend simply results from a selection effect. Padovani 2007 proposed three tests that would prove the observed trend has a real physical basis: (i) the existence of an anti-correlation between the synchrotron peak frequency and the bolometric observed luminosity; (ii) the absence of outliers from the correlation; (iii) and higher intrinsic numbers of high-frequency-peaked

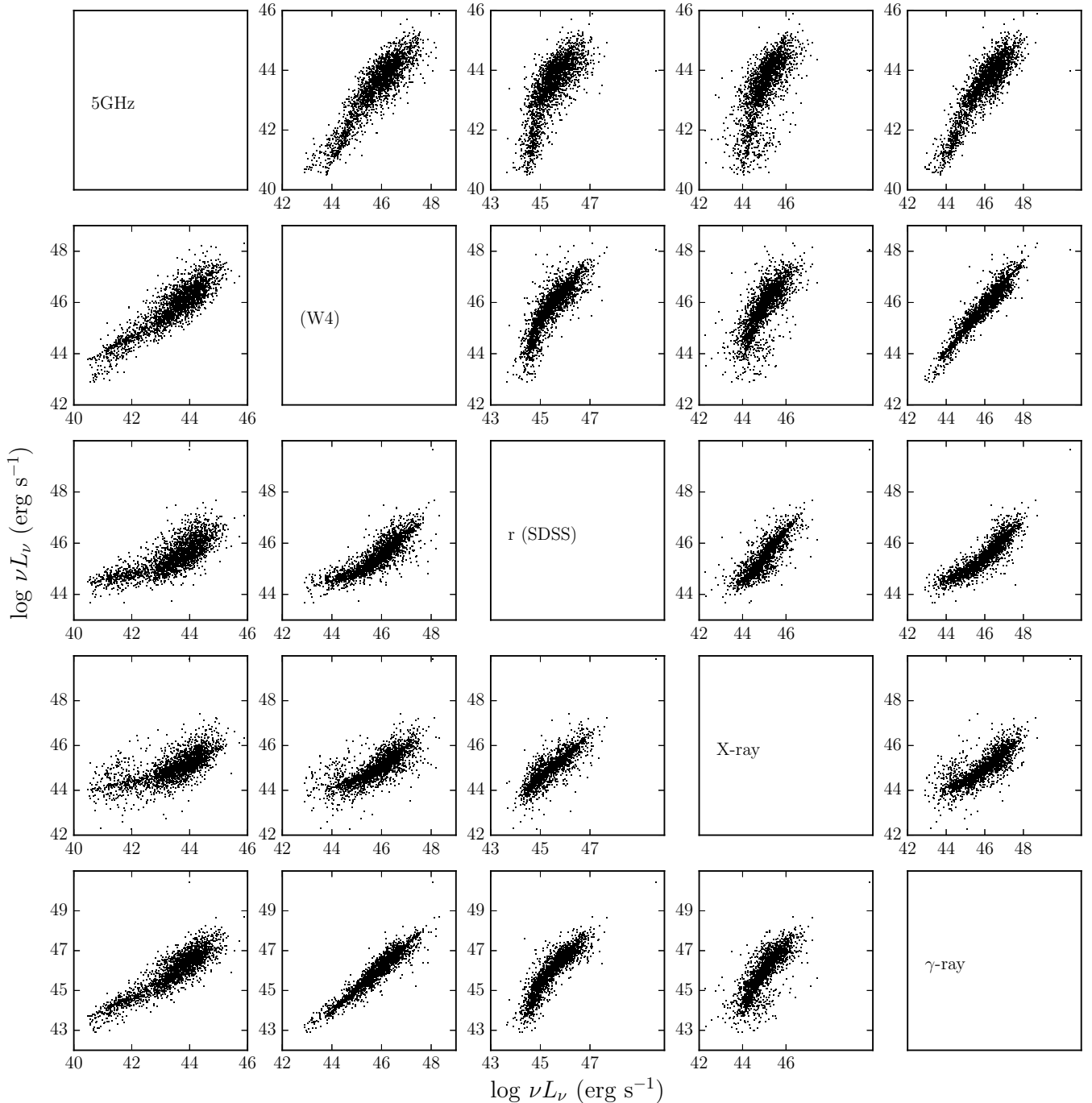


FIG. 11.— KNN pairs plots with imputed data. The general linear trends are conserved in all cases.

blazars relative to low-frequency-peaked ones. Here we addressed the first test, showing through principal component analysis that the trend involves the overall luminosity (at all wavelengths sampled). Furthermore, we checked that the correlation does not simply result from the common redshift dependence of luminosity at any wavelength known as (the “common-distance bias”, Pavlidou et al. 2012). In particular, we permuted the redshifts among the blazars and re-calculated luminosities at each wavelength; after intensive bootstrapping, we found that the probability of measuring the correla-

tion coefficient and slope we observe is less than 0.1%. We also tried assigning each blazar a random redshift from the observed distribution (instead of permuting the observed ones); the probability of getting the observed correlation was again less than 0.1%. Therefore, while redshift does introduce some correlation in luminosity space when none exists, the level of correlation seen in our sample is certainly driven by the redshift distribution, thus being real under the assumption that our sample is representative of the whole blazar population.

The SED estimator we present forms the basis of a

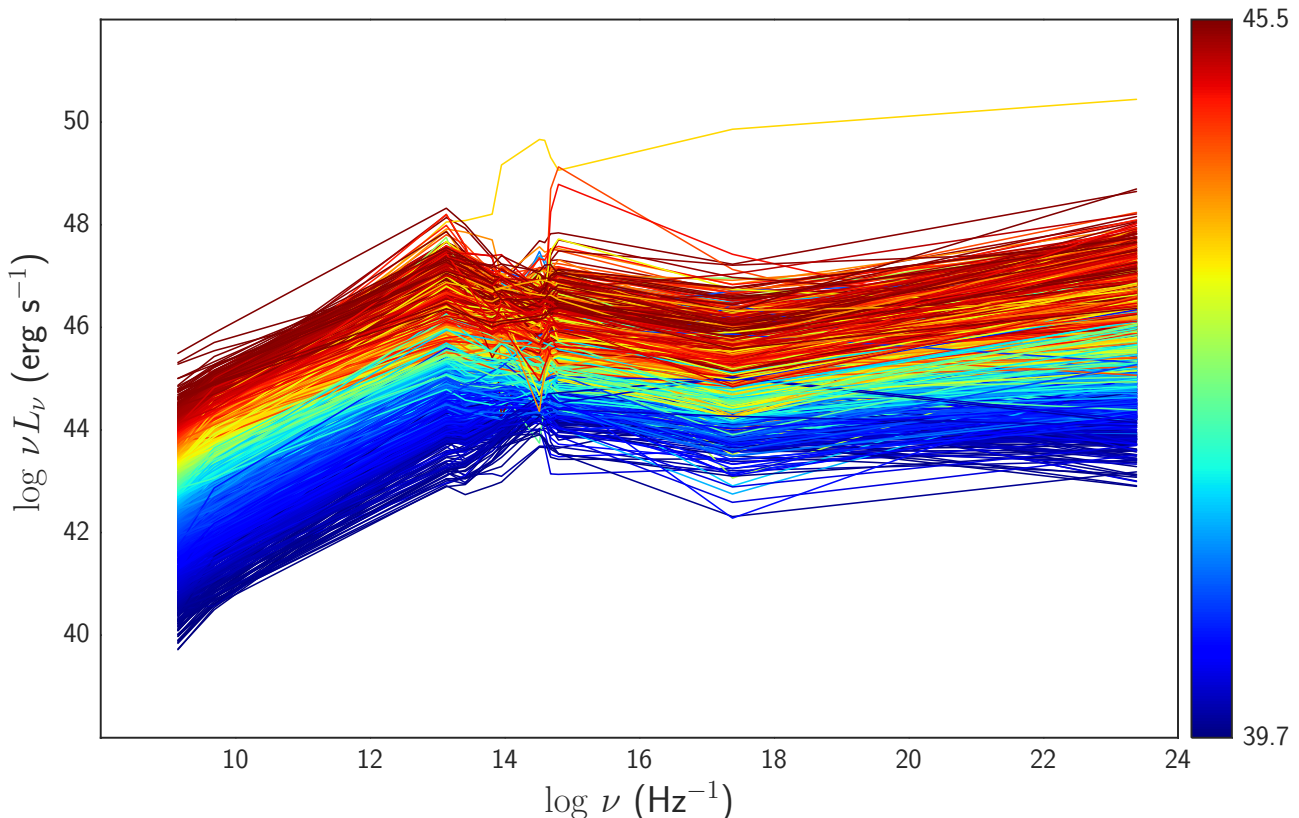


FIG. 12.— SEDs of the full sample of 2214 blazars, similar to Fig. 8 but including KNN-imputed data. The least-complete data (blazars with only radio flux) are plotted first then blazars with increasingly complete SEDs, such that the most-complete data (blazars with fluxes in every band) are plotted last (i.e., on top of the other curves). Data points are connected with straight lines among the 12 bands. There is much scatter but the synchrotron peak still decreases in frequency, and the  $\gamma$ -ray dominance increases, with increasing luminosity.

detailed Monte-Carlo simulation to probe the true volume densities of blazars, i.e., to answer precisely whether high-frequency-peaked blazars are indeed more numerous than low-frequency-peaked blazars (Mao et al., in prep.) — the third test mentioned above. Another paper (Mao et al., in prep.) tests whether the blazars missing redshifts are preferentially high-redshift, high-frequency-peaked BL Lac objects, i.e., the outliers identified in the second test mentioned above. So far, the first test — of an intrinsic correlation between bolometric luminosity and SED shape — supports the intrinsic nature of the blazar sequence.

## 6. ACKNOWLEDGMENTS

This publication makes use of data products from the Wide-field Infrared Survey Explorer, which is a joint project of the University of California, Los Angeles, and the Jet Propulsion Laboratory/California Institute of Technology, funded by the National Aeronautics and Space Administration.

This work made use of data supplied by the UK Swift Science Data Centre at the University of Leicester.

Funding for SDSS-III has been provided by the Alfred P. Sloan Foundation, the Participating Institutions, the National Science Foundation, and the U.S. Department of Energy Office of Science. The SDSS-III web site is <http://www.sdss3.org/>. SDSS-III is managed by the Astrophysical Research Consortium for the Participating Institutions of the SDSS-III Collaboration includ-

ing the University of Arizona, the Brazilian Participation Group, Brookhaven National Laboratory, Carnegie Mellon University, University of Florida, the French Participation Group, the German Participation Group, Harvard University, the Instituto de Astrofísica de Canarias, the Michigan State/Notre Dame/JINA Participation Group, Johns Hopkins University, Lawrence Berkeley National Laboratory, Max Planck Institute for Astrophysics, Max Planck Institute for Extraterrestrial Physics, New Mexico State University, New York University, Ohio State University, Pennsylvania State University, University of Portsmouth, Princeton University, the Spanish Participation Group, University of Tokyo, University of Utah, Vanderbilt University, University of Virginia, University of Washington, and Yale University.

Part of this work is based on archival data, software or on-line services provided by the ASI Science Data Center.

This research has made use of data obtained from the high-energy Astrophysics Science Archive Research Center (HEASARC) provided by NASA’s Goddard Space Flight Center;

The NASA/IPAC Extragalactic Database (NED) operated by the Jet Propulsion Laboratory, California Institute of Technology, under contract with the National Aeronautics and Space Administration.

TOPCAT<sup>12</sup> (Taylor 2005) for the preparation and manipulation of the tabular data and the images.

<sup>12</sup> <http://www.star.bris.ac.uk/~mbt/topcat/>



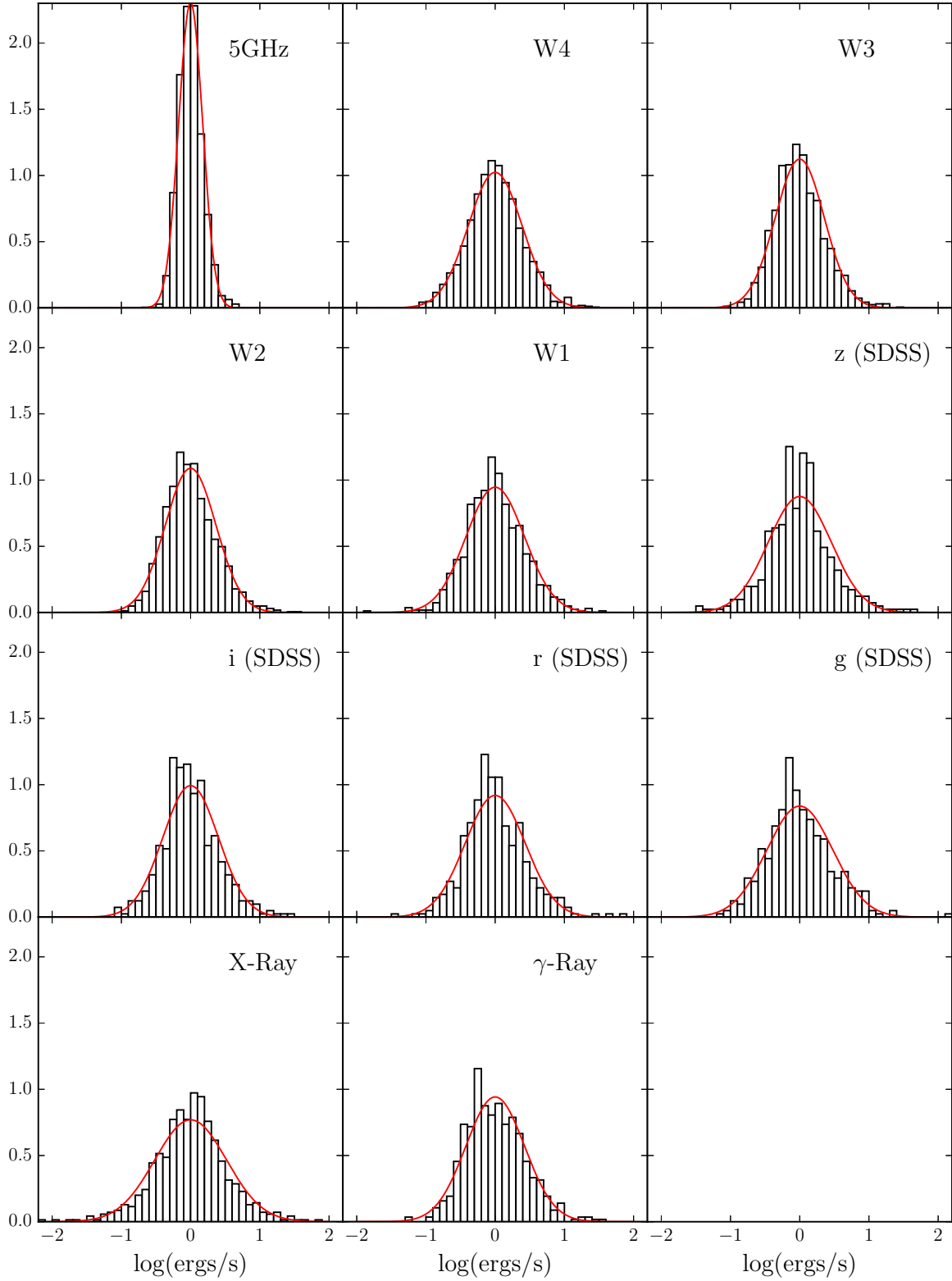


FIG. 13.— Residuals of the estimator with coefficients given in Table 9, using redshift and 1.4-GHz radio luminosity as inputs. These are distributed around zero, with Gaussian half-widths of 1 sigma, where the  $x$ -axis is the difference between the predicted value and the data value (difference in  $\log(\nu L_\nu)$ ); the total area is normalized to unity.

The work by is supported by the Programma Giovani Ricercatori - Rita Levi Montalcini - Rientro dei Cervelli (2012). This review is also supported by the NASA grants NNX12AO97G and NNX13AP20G.

F.M. is in debt with Dr. D'Abrusco for all the valuable discussions.

## REFERENCES

- Abdo, A. A., Ackermann, M., Agudo, I., et al. 2010, *ApJ*, 716, 30
- Acerro, F., Ackermann, M., Ajello, M., et al. 2015, *ApJS*, 218, 23
- Ackermann, M., Ajello, M., Allafort, A., et al. 2011, *ApJ*, 743, 171
- Ahn, C. P., Alexandroff, R., Allende Prieto, C., et al. 2012, *ApJS*, 203, 21
- Angel, J. R. P., & Stockman, H. S. 1980, *ARA&A*, 18, 321
- Atwood, W. B., Abdo, A. A., Ackermann, M., et al. 2009, *ApJ*, 697, 1071
- Becker, R. H., White, R. L., & Helfand, D. J. 1995, *ApJ*, 450, 559
- Blandford, R. D., & Rees, M. J. 1978, *Phys. Scr*, 17, 265
- Burrows, D. N., Hill, J. E., Nousek, J. A., et al. 2005, *Space Sci. Rev.*, 120, 165
- Chen, L., & Bai, J. M. 2011, *ApJ*, 735, 108
- Condon, J. J., Cotton, W. D., Greisen, E. W., et al. 1998, *AJ*, 115, 1693
- D’Abrusco, R., Massaro, F., Paggi, A., et al. 2013, *ApJS*, 206, 12
- , 2014, *ApJS*, 215, 14
- Donato, D., Ghisellini, G., Tagliaferri, G., & Fossati, G. 2001, *A&A*, 375, 739
- Draine, B. T. 2003, *ARA&A*, 41, 241
- Evans, P. A., Osborne, J. P., Beardmore, A. P., et al. 2014, *ApJS*, 210, 8
- Feigelson, E. D., & Jogesh Babu, G. 2012, *Modern Statistical Methods for Astronomy*
- Fichtel, C. E., Bertsch, D. L., Chiang, J., et al. 1994, *ApJS*, 94, 551
- Fossati, G., Celotti, A., Ghisellini, G., & Maraschi, L. 1997, *MNRAS*, 289, 136
- Fossati, G., Maraschi, L., Celotti, A., Comastri, A., & Ghisellini, G. 1998, *MNRAS*, 299, 433
- Ghisellini, G., Celotti, A., Fossati, G., Maraschi, L., & Comastri, A. 1998, *MNRAS*, 301, 451
- Ghisellini, G., Maraschi, L., & Tavecchio, F. 2009, *MNRAS*, 396, L105
- Ghisellini, G., & Tavecchio, F. 2008, *MNRAS*, 387, 1669
- Ghisellini, G., Tavecchio, F., Foschini, L., et al. 2012, *MNRAS*, 425, 1371
- Ghisellini, G., Tagliaferri, G., Foschini, L., et al. 2011, *MNRAS*, 411, 901
- Giommi, P., Menna, M. T., & Padovani, P. 1999, *MNRAS*, 310, 465
- Giommi, P., & Padovani, P. 1994, *MNRAS*, 268, L51
- Giommi, P., Padovani, P., & Polenta, G. 2013, *MNRAS*, 431, 1914
- Giommi, P., Padovani, P., Polenta, G., et al. 2012, *MNRAS*, 420, 2899
- Hinshaw, G., Larson, D., Komatsu, E., et al. 2013, *ApJS*, 208, 19
- Kalberla, P. M. W., Burton, W. B., Hartmann, D., et al. 2005, *A&A*, 440, 775
- Landt, H., Padovani, P., Perlman, E. S., et al. 2001, *MNRAS*, 323, 757
- Maraschi, L., Ghisellini, G., Tanzi, E. G., & Treves, A. 1986, *ApJ*, 310, 325
- Massaro, E., Giommi, P., Leto, C., et al. 2011a, *Multifrequency Catalogue of Blazars (3rd Edition)*
- , 2009, *A&A*, 495, 691
- Massaro, E., Maselli, A., Leto, C., et al. 2014a, *Multifrequency Catalogue of Blazars - 5th Edition*
- Massaro, E., Nesci, R., & Piranomonte, S. 2012, *MNRAS*, 422, 2322
- Massaro, F., D’Abrusco, R., Giroletti, M., et al. 2013, *ApJS*, 207, 4
- Massaro, F., Masetti, N., D’Abrusco, R., Paggi, A., & Funk, S. 2014b, *AJ*, 148, 66
- Massaro, F., Paggi, A., Elvis, M., & Cavaliere, A. 2011b, *ApJ*, 739, 73
- Massaro, F., Tramacere, A., Cavaliere, A., Perri, M., & Giommi, P. 2008, *A&A*, 478, 395
- Mauch, T., Murphy, T., Buttery, H. J., et al. 2003, *MNRAS*, 342, 1117
- Meyer, E. T., Fossati, G., Georganopoulos, M., & Lister, M. L. 2011, *ApJ*, 740, 98
- Mukai, K. 1993, *Legacy*, vol. 3, p.21-31, 3, 21
- Nieppola, E., Tornikoski, M., & Valtaoja, E. 2006, *A&A*, 445, 441
- Nieppola, E., Valtaoja, E., Tornikoski, M., Hovatta, T., & Kotiranta, M. 2008, *A&A*, 488, 867
- Padovani, P. 2007, *Ap&SS*, 309, 63
- Pavlidou, V., Richards, J. L., Max-Moerbeck, W., et al. 2012, *ApJ*, 751, 149
- Plotkin, R. M., Anderson, S. F., Brandt, W. N., et al. 2012, *ApJ*, 745, L27
- Sambruna, R. M., Maraschi, L., & Urry, C. M. 1996, *ApJ*, 463, 444
- Shields, G. A. 1978, *Nature*, 272, 706
- Stocke, J. T., Liebert, J., Schmidt, G., et al. 1985, *ApJ*, 298, 619
- Stoughton, C., Lupton, R. H., Bernardi, M., et al. 2002, *AJ*, 123, 485
- Taylor, M. B. 2005, in *Astronomical Society of the Pacific Conference Series*, Vol. 347, *Astronomical Data Analysis Software and Systems XIV*, ed. P. Shopbell, M. Britton, & R. Ebert, 29
- Urry, C. M., & Mushotzky, R. F. 1982, *ApJ*, 253, 38
- Urry, C. M., & Padovani, P. 1995, *PASP*, 107, 803
- White, R. L., Becker, R. H., Helfand, D. J., & Gregg, M. D. 1997, *ApJ*, 475, 479
- Wright, E. L., Eisenhardt, P. R. M., Mainzer, A. K., et al. 2010, *AJ*, 140, 1868